scientific reports

Check for updates

OPEN

Individual domain characteristics determined by second-harmonic generation diffractometer for multi-domain multiferroics

Young Jin Jeong[1], Do Gyeom Jeong[1], Hwiin Ju[1], In Hyeok Choi[1], Chang Jae Roh[1], Jin Hong Lee[2], Chan-Ho Yang[2] & Jong Seok Lee[1]✉

We investigated the multi-domain states of a multiferroic La-doped $BiFeO_3$ (BLFO) thin film by examining diffraction patterns in optical second-harmonic generation (SHG) measurement. By directing a laser onto the domain wall within the domain-patterned sample, we observed clear diffraction signatures of SHG waves generated from two ferroelectric domains. We explained the experimental results of the diffraction patterns, including the intensity distribution and the polarization characteristics, using Fresnel propagation of SHG waves. From this, we could determine the amplitude and phase of the SHG waves generated from each domain, and figure out not only the polarization direction of each ferroelectric domain but also the phase related to the complex-valued second-order susceptibility tensor. Consequently, we could present SHG diffractometry as an effective measurement method to reveal the phase details of electric polarization of the multi-domain states of ferroic materials.

Ferroelectric materials have been extensively studied for their applications in non-volatile memory[1], optoelectric devices[2], and so on by exploiting a large spontaneous polarization as well as an excellent controllability of the electric polarization. Whereas multi-domain states are often formed to reduce the electrostatic energy, achieving a precise understanding of an individual domain is paramount to fully exploit the ferroelectric polarization. Optical second-harmonic generation (SHG) measurement serves as one of the most powerful techniques to characterize the electrical polarization of ferroelectric materials. As a leading-order electric dipole contribution to the SHG process is allowed only in the inversion-symmetry-broken phase, the SHG method can give useful information about the electrical polarization of ferroelectricity based on the anisotropic characteristics related to the ferroelectric polarization[3–8]. By the way, when the ferroelectric domain is smaller than the light spot size, second-harmonic (SH) light generated from each domain becomes mixed, and hence accurate information about the single domain would be elusive. Also, as conventional SHG measurements usually track the intensity of the SH wave, the phase information of SH light is lost, hindering an appropriate extraction of the polarization information of ferroelectric domains.

Efforts to surpass the limitations of the SHG technique continue to improve the spatial resolution, particularly by exploiting the near-field interaction[9], and also to obtain phase information from the interference of SH waves[10]. In particular, numerous methods have been demonstrated utilizing different configurations of phase shift units and reference materials[11–13]. These include methods involving a pressure adjustment using a gas cell[14,15], a distance adjustment between the sample and reference material, a placement of glass or fused silica between the sample and reference material to create a path difference[16–18], and a use of a pair of wedges to control phase shift[19]. Additionally, methods involving phase modulator-connected oscillators and wave plates have also been explored[20]. By the way, as these measurement methods often rely on a comparison with results from an external reference, it is crucial to have accurate information about the reference material's polarization to determine that of the target sample.

In this work, we demonstrate that a far-field SHG diffraction from a multi-domain state can be useful in extracting polarization information of individual domains without relying on the reference measurement. By focusing the fundamental wave onto the domain boundary formed between two domains, we generate the SH waves from both domains, which propagate in a free space and interfere with each other. We characterize the

[1]Department of Physics and Photon Science, Gwangju Institute of Science and Technology (GIST), Gwangju 61005, Republic of Korea. [2]Department of Physics, Korea Advanced Institute of Science and Technology (KAIST), 291 Daehak-ro, Yuseong-gu, Daejeon 34141, Republic of Korea. ✉email: jsl@gist.ac.kr

spatial distribution of the diffraction patterns as well as the position-dependent polarization states of the SH waves. From these experimental results of SHG diffraction, we could provide useful information about the polarization axes of each domain and the phase related to the nonlinear susceptibility.

Results

To investigate how multi-domains would influence the SHG responses, we prepared well-defined patterns of ferroelectric domains in the $Bi_{0.95}La_{0.05}FeO_3$ (BLFO) film grown on the $LaAlO_3$ substrate. The BLFO has the monoclinic structure for both tetragonal-like and rhombohedral-like phases, which belong to the space group *Cm* (or *Cc*) and *Pm* (or *Pc*)[21]. Note that all these space groups correspond to the point group *m*. The two structural phases have ferroelectric polarizations along 60° and 43°, respectively, with respect to the [100] axis[22]. In Fig. 1a, each nano-domain appears as a tilted stripe shape with a width of a few nm. There are two super-domains whose areas are indicated by blue (domain 1) and red lines (domain 2). Figures 1b, c display the schematics of polarization directions in each single domain together with the net polarization of the super-domain. Provided that relative populations of nano-domains would be the same, domain 1 and 2 should exhibit a mirror symmetry with respect to the domain boundary oriented perpendicular to the [100] direction (*x*-axis) of $LaAlO_3$, indicated with a white horizontal arrow. As this multi-domain ferroelectric material contains well-defined inversion-symmetry-broken domains, it can be a good testbed for studying and employing the diffraction properties of SH light.

We first examined the second harmonic response from the individual super-domain of BLFO. Figure 1d displays the SHG intensity distribution obtained over the entire region of super-domains. Here, the fundamental and second-harmonic waves are set to have the same polarization in parallel to [100]. The mapping result reveals two distinct regions that coincide with the domain distribution initially patterned. Although the chiral-type domain wall can act as a strong SHG source[23], we do not find a meaningful response at the domain wall, and hence exclude a possible SHG contribution from the domain wall in further discussions. Figures 1e, f display the SHG intensity of each domain obtained with a variation of the analyzer angle. Here, the input laser polarization direction is set to be along the *x*-axis. Both domains exhibit two-fold anisotropic responses having the two-fold axis along 115° and 45°, respectively. Importantly, this two-fold pattern is directed similarly to the net polarization of each super-domain, as indicated by thick blue and red arrows in Figs. 1b, c, respectively. Note that the net polarization of the super-domain is determined by a relative population of nano-domains of tetragonal-like and rhombohedral-like phase, of which polarization configurations were controlled by lateral piezoresponse force microscopy (PFM) by rotating the direction of the cantilever[22]. And, it should be emphasized that this correspondence is valid as the size of constituent nano-domains is much smaller than the wavelength of

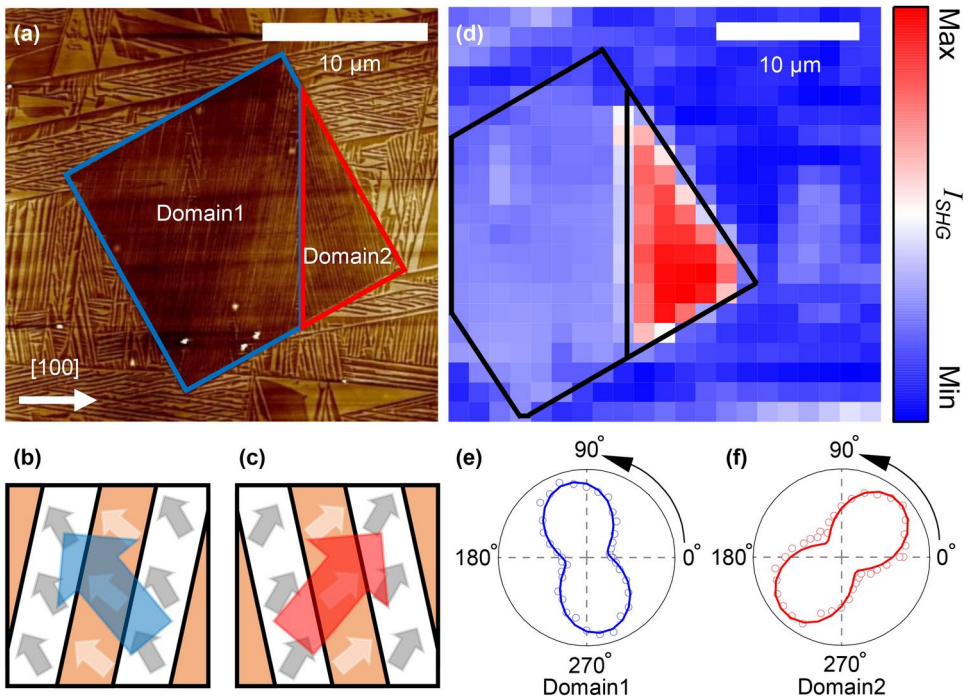

Fig. 1. La-doped $BiFeO_3$ (BLFO) with multiferroic domains. (**a**) Atomic force microscopy results of domain-patterned BLFO. Blue and red boxes indicate domains 1 and 2, respectively, where nanometer-wide stripe domains are also visible. (**b**,**c**) Schematic illustrations of stripe patterns of domains 1 and 2. Arrows denote polarization directions in each super-domain (large arrows) and single domain (small arrows). Note that the polarization directions can be oppositely given for each domain. (**d**) Distribution of the second-harmonic generation intensity. Two domains are well discernible. (**e**,**f**) SHG intensity patterns obtained by rotating the analyzer for domains 1 and 2. Dots represent experimental results, and lines denote SHG fitting data.

laser used in the SHG measurement; the SHG light emitted from each nano-domain is coherently summed contributing to the final SHG intensity.

To further address the multi-domain contribution to the SHG responses, we locate the fundamental wave at the boundary formed between two super-domains, and check the characteristics of the second harmonic wave. Here, the fundamental beam has a diameter of ~ 2 μm, and its polarization direction is set to be *x*-axis, being perpendicular to the direction of the domain wall. As shown in Fig. 2a, SH waves emitted from each domain propagate and interfere with each other when a detection is made. To study these interference patterns in detail, we map the SHG intensity distribution by moving a 30 μm-diameter pinhole located between the pinhole and the detector and at 60 cm behind the sample. We also characterize the polarization state of the SH wave at each pinhole position using a linear polarizer (analyzer). Two representative results of our SHG diffractometry, obtained with the analyzer angle $\theta = 0°$ and 90°, are shown in Figs. 2b, c, respectively. At $\theta = 0°$, which corresponds to the polarization direction of incident light, we observed a beam splitting into two distinct components, indicating a presence of the diffraction phenomenon. Conversely, at $\theta = 90°$, the beam remains undivided, signifying an absence of the diffraction. These polarization-dependent diffraction patterns are understood by considering the ferroelectric polarization directions of two domains. Along the vertical direction, two super-domains have a common polarization component and should behave identically. Therefore, the SHG wave propagates maintaining the shape of the fundamental wave, which has the Gaussian shape, as detected. Along the horizontal direction, however, two super-domains have opposite orientations of the ferroelectric polarizations, and hence there should be a phase difference of 180°. The beam splitting observed at a specific analyzer angle conclusively confirms the existence of diffraction effects in our SHG experiments for the multi-domain state.

Figure 3a presents the distribution of the SHG intensity obtained by moving the 30 μm-diameter pinhole with a 300 μm moving step with a variation of the analyzer angle θ from 0° to 180°. Consistently with the results in Fig. 2, well-separated diffraction peaks are observed for the horizontal polarization, namely at $\theta = 0°$ and 180°, and a single-peaked pattern is observed for the vertical polarization, namely at $\theta = 90°$. Interestingly, the distributions obtained at intermediate angles exhibit unbalanced separations in the beam shapes; both results at $\theta = 20°$ and 160° show that one side of the split peaks is much stronger than the other. For a more quantitative understanding, we introduce two parameters representing the beam separation and the asymmetry in the distribution as $\sum_{x_R} |x_R|\, I(x_R)/I_R + \sum_{x_L} |x_L|\, I(x_L)/I_L$ and $(I_L - I_R)\,/\,(I_L + I_R)$, respectively. Here, x_L and x_R measure the pinhole position on the left and right sides of the *x*-axis relative to $x = 0$, and I_L and I_R are the total SHG intensity on the left and right sides, respectively. According to this definition, the minimum value of the beam separation corresponds to the full-width-at-half-maximum of the single-Gaussian distribution at $\theta = 90°$. As presented in Figs. 3b, c, both parameters exhibit systematic variations as a function of the analyzer angle, which we will fit based on the model analysis.

In Fig. 3d, we present another important experimental result showing the position-dependent polarization characteristics of the SHG wave. Here, the analyzer-angle-dependent SHG patterns are obtained with a pinhole position varied horizontally from − 1.2 mm to 1.2 mm with its vertical position fixed at the center. All the SHG results exhibit a clear two-fold anisotropic response, indicating the linear polarization state of the second-harmonic wave at each pinhole position. However, the polarization axis shows a significant and systematic change as a function of the pinhole position *x*. While the SH waves at both ends ($x = \pm 1.2$ mm) are horizontally polarized, those at the center ($x = 0$ mm) are vertically polarized. As *x* varies, the polarization axis rotates between horizontal and vertical directions. These behaviors also clearly indicate the diffraction of SH waves from two super-domains, as demonstrated in the below.

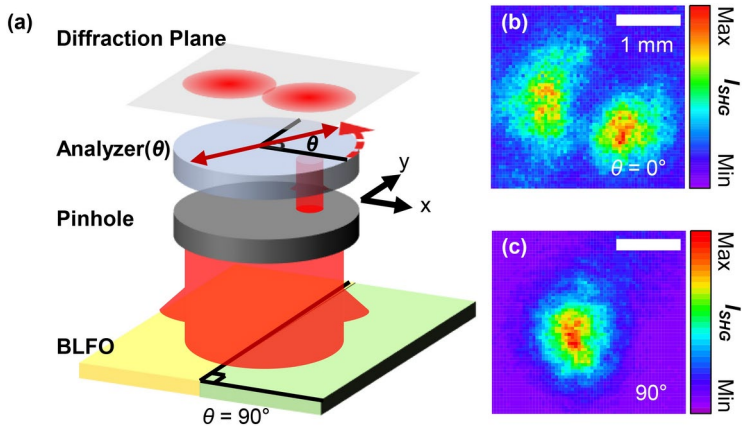

Fig. 2. Schematic of SHG diffraction experiment and representative results. (**a**) Propagation of SHG waves from two domains through a pinhole and analyzer before its detection. The pinhole segments the SHG wave, allowing a characterization of the SHG intensity distribution and the position-dependent polarization characteristic. (**b**,**c**) Mapping of the SHG intensity obtained at an analyzer angle $\theta = 0°$ (**b**) and 90° (**c**).

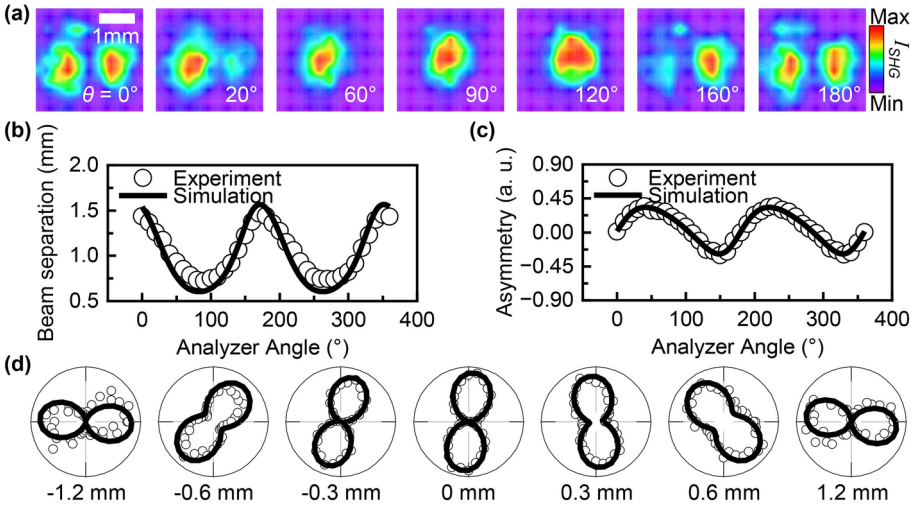

Fig. 3. Experimental results of SHG diffractions and simulation lines. (**a**) SHG mapping results obtained with a variation of the analyzer angle θ. A beam splitting is observed at $\theta = 0°$ and 180°, and an unbalanced beam separation is seen at $\theta = 20°$ and 160°. (**b**,**c**) Beam separation and asymmetry as a function of θ. Definitions of two parameters are given in the main text. (**d**) Position-dependent polarization characteristics of the SHG wave. In (**b**), (**c**), and (**d**), dots and lines are experimental and simulation results, respectively.

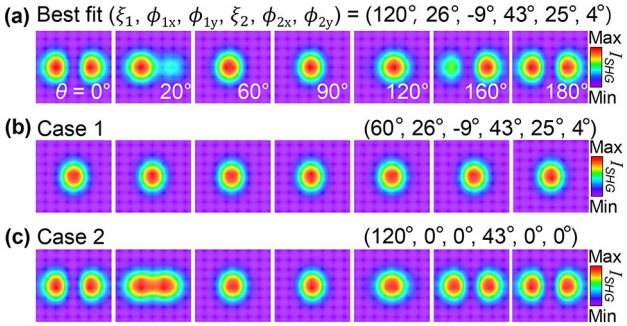

Fig. 4. Simulation results of the SHG diffraction patterns by varying amplitude and phase of SHG waves generated from two domains. (**a**) Best fit result of the SHG intensity distribution. (**b**,**c**) The SHG intensity distributions obtained with controlled amplitude and phase parameters conditions. Parameters used for each fitting are shown for the amplitude ξ and phase ϕ of the electric field. The area of each mapping is 3×3 mm^2.

From now on, we explain the simulation results of the SH response of the multi-domain state by considering the free space wave propagation of the SH waves from two adjacent super-domains. As aforementioned, we exclude the SH wave generated directly from the domain wall. Also, we ignore additional multiple-reflection contributions in our thin film geometry as the reflectivity from the film-substrate interface is sufficiently low as about 0.03 and 0.05 at 800 nm and 400 nm, respectively[24,25]. We first define the SH electric field of each domain $\vec{E}_1(2\omega)$ and $\vec{E}_2(2\omega)$ as

$$\vec{E}_1(2\omega) = \begin{pmatrix} \cos(\xi_1)\, e^{i\phi_{1x}} \\ \sin(\xi_1)\, e^{i\phi_{1y}} \end{pmatrix}, \vec{E}_2(2\omega) = \begin{pmatrix} \cos(\xi_2)\, e^{i\phi_{2x}} \\ \sin(\xi_2)\, e^{i\phi_{2y}} \end{pmatrix}. \quad (1)$$

Here, we allow the x- and y-component electric fields to have relatively different amplitudes by using $\xi_{1,2}$ term; for example, $\xi_{1,2} = 0°$ and 90° correspond to the horizontal and vertical polarization directions, respectively. Also, each electric field component can have its own phase represented by ϕ. Additionally, a spatial amplitude distribution of each electric field takes a half-Gaussian to mimic the experimental situation where the fundamental wave illuminates the sample with its central position located at the domain boundary. Then we propagate each wave following Fresnel's law and allow them to interfere with each other at the detection position. By varying the amplitude and phase factors defined in this formalism, we fit the experimental results shown in Fig. 3, including the θ-dependent beam separation and asymmetry.

Figure 4a displays an intensity distribution obtained by using parameters that best fit experimental results shown in Fig. 3. Evolutions of the beam separation and asymmetry can be well reproduced, as can be seen with solid lines in Figs. 3b, c. Furthermore, as shown in Fig. 3d, the simulation results reproduce quite well

the position-dependent change in the polarization axis of the second harmonic wave. Fitting parameters are summarized as $(\xi,\phi_x,\phi_y)=(120°, 26°, -9°)$ and (43°, 25°, 4°) for the domain 1 and 2, respectively. These parameters suggest that the second harmonic wave is elliptically polarized with a major polarization axis can be perfectly reproduced using these parameters. This comparison demonstrates the validity of our approach based on the SHG diffraction to extract information of the individual domain. Before discussing the scientific implication of these fitting results, let us discuss how sensitively the fitting results are influenced by variations in parameters of ξ and ϕ. First, we adjust the amplitude parameter $\xi_{1,2}$ which represents the SHG polarization directions of the ferroelectric domain. In Fig. 4b, we set $\xi_1 = 60°$ which now becomes similar to $\xi_2 = 45°$. In this case, as the polarization directions of two SH waves are similar, two waves behave similarly, and no clear beam separation is observed, as expected. Second, we adjust the phase values to zero in Fig. 4c. In this case, although the beam separation is clearly observed, the intensity splitting appears always symmetrically. This confirms that the finite phase term should be included to account for the experimental results. A further examination with a finer tuning of the phase term reveals that both domains likely have similar values of ϕ_x and ϕ_y as found in the best-fitting results (Supplementary Information).

Importantly, the parameters used for this successful fit can provide useful information about the polarization states of each domain; the obtained $\xi_1 = 120°$ and $\xi_2 = 43°$ are well consistent with the polarization directions determined for each super-domain, which were 115° and 45° (Figs. 1e, f), respectively. Interestingly, the phase terms $\phi_{1,2}$ are given as non-zero values, and they are similar for both domains; the *x*- and *y*-component of SH electric fields have a phase difference of about 30°. As the present SHG experiment was executed in a normal-incidence reflection geometry, we can ignore a finite difference in the Fresnel coefficients between s- and p-polarized waves defined in an oblique incidence geometry. Instead, it would be possible that the in-plane anisotropy can contribute to the difference in the phase factors for the *x*- and *y*-component waves. It should also be noted that the energy band gap of BFO is about 2.6–3.0 eV[26], which is smaller than the energy of the SH wave. This suggests that the optical constants, including the second-order nonlinear susceptibility tensors, can be complex-valued, and hence the additional phase difference is naturally expected, particularly when there would be a finite in-plane anisotropy.

In summary, our research delved into the multi-domain states of a multiferroic BLFO thin film by examining diffraction patterns in optical second-harmonic generation (SHG) measurement. By collecting SHG waves generated from two ferroelectric domains forming a well-defined domain boundary, we observed clear diffraction signatures of the SHG wave in its position- and polarization-dependent distributions. By scrutinizing these diffraction patterns, we successfully interpreted the experimental findings using a Fresnel propagation model of SHG waves with an anisotropic phase difference. Importantly, we could provide useful information about the polarization direction of each ferroelectric domain and the phase related to the complex-valued second-order susceptibility tensor. Consequently, we could present SHG diffractometry as a useful measurement method to reveal the phase details of electric polarization of the multi-domain states of ferroic materials without relying on the additional reference measurement.

Method

Sample preparation

Thin films of La(5%)-substituted $BiFeO_3$ ($Bi_{0.95}La_{0.05}FeO_3$, BLFO) were deposited on (001) $LaAlO_3$ substrates with a conducting buffer layer of $Pr_{0.5}Ca_{0.5}MnO_3$ using pulsed laser deposition employing a KrF (krypton fluoride laser) excimer laser ($\lambda = 248$ nm). During the pulsed laser deposition process, a BLFO ceramic target with an excess of Bi by 10% was utilized to prevent bismuth loss. The laser had an energy and frequency of 100 mJ and 10 Hz, respectively. The substrate temperature was maintained at 650 °C, and the oxygen partial pressure was set to 100 mTorr during growth. After the completion of the growth process, the samples were gradually cooled to room temperature at a rate of 10 °C per min in an oxygen environment with a pressure of 500 Torr. The thickness of the BLFO film was approximately 60 nm. By employing electric fields generated by a DC-biased atomic force microscope tip, we generated and manipulated the tetragonal-like and rhombohedral-like ferroelectric domains to have a well-defined domain pattern[22].

Optical second-harmonic generation measurement

An 800 nm laser with a power of 2 mW and a repetition rate of 80 MHz was modulated to 700 Hz using a chopper, and it was focused onto the sample using an objective lens (40×, numerical aperture 0.65). A pinhole with a 30 μm diameter was positioned behind 60 cm away from the sample, and its position was raster-scanned to map the distribution of the SHG intensity. Also, a linear polarizer is introduced to analyze the polarization state of the SHG wave. The fundamental wave is filtered out using a short-pass filter and band-pass filter, and the SHG intensity is acquired with a photomultiplier tube connected to the lock-in amplifier.

Data availability

The data that support the findings of this study are available from the corresponding author J. S. L., upon reasonable request.

Received: 24 July 2024; Accepted: 7 October 2024
Published online: 16 October 2024

References

1. Guo, R. et al. Non-volatile memory based on the ferroelectric photovoltaic effect. *Nat. Commun.* **4**, 1990. https://doi.org/10.1038/ncomms2990 (2013).

2. Chen, J.-W. et al. A gate-free monolayer WSe2 pn diode. *Nat. Commun.* **9**, 3143. https://doi.org/10.1038/s41467-018-05326-x (2018).
3. Sharan, A. et al. Bismuth manganite: A multiferroic with a large nonlinear optical response. *Phys. Rev. B* **69**, 214109. https://doi.org/10.1103/PhysRevB.69.214109 (2004).
4. Yokota, H., Haumont, R., Kiat, J.-M., Matsuura, H. & Uesu, Y. Second harmonic generation microscopic observations of a multiferroic $BiFeO_3$ single crystal. *Appl. Phys. Lett.* **95**, 082904. https://doi.org/10.1063/1.3212729 (2009).
5. Roh, C. J., Lee, J. H., Kim, K.-E., Yang, C.-H. & Lee, J. S. Deterministic domain reorientations in the $BiFeO_3$ thin film upon the thermal phase transitions. *Appl. Phys. Lett.* **113**, 052904. https://doi.org/10.1063/1.5040726 (2018).
6. Barad, Y. et al. Probing domain microstructure in ferroelectric $Bi_4Ti_3O_{12}$ thin films by optical second harmonic generation. *J. Appl. Phys.* **89**, 1387–1392. https://doi.org/10.1063/1.1334641 (2001).
7. Narayanan, A. et al. Ferroelectric polarization and second harmonic generation in supramolecular cocrystals with two axes of charge-transfer. *J. Am. Chem. Soc.* **139**, 9186–9191. https://doi.org/10.1021/jacs.7b02279 (2017).
8. Ju, H. et al. Possible persistence of multiferroic order down to bilayer limit of van der Waals material NiI_2. *Nano Lett.* **21**, 5126–5132. https://doi.org/10.1021/acs.nanolett.1c01095 (2021).
9. Yeh, C. H., Tan, C. Z., Cheng, C. A., Hung, J. T. & Chen, S. Y. Improving resolution of second harmonic generation microscopy via scanning structured illumination. *Biomed. Opt. Express* **9**, 6081–6090. https://doi.org/10.1364/boe.9.006081 (2018).
10. Kim, W., Ahn, J. Y., Oh, J., Shim, J. H. & Ryu, S. Second-harmonic Young's interference in atom-thin heterocrystals. *Nano Lett.* **20**, 8825–8831. https://doi.org/10.1021/acs.nanolett.0c03763 (2020).
11. Stolle, R., Marowsky, G., Schwarzberg, E. & Berkovic, G. Phase measurements in nonlinear optics. *Appl. Phys. B Laser Opt.* **63**, 491–498. https://doi.org/10.1007/bf01828946 (1996).
12. LuPke, G., Marowsky, G. & Steinhoff, R. Phase-controlled nonlinear interferometry. *Appl. Phys. B Photophys. Laser Chem.* **49**, 283–289. https://doi.org/10.1007/bf00714649 (1989).
13. Denev, S. A., Lummen, T. T. A., Barnes, E., Kumar, A. & Gopalan, V. Probing ferroelectrics using optical second harmonic generation. *J. Am. Ceram. Soc.* **94**, 2699–2727. https://doi.org/10.1111/j.1551-2916.2011.04740.x (2011).
14. Chang, R. K., Ducuing, J. & Bloembergen, N. Relative phase measurement between fundamental and second-harmonic light. *Phys. Rev. Lett.* **15**, 6–8. https://doi.org/10.1103/PhysRevLett.15.6 (1965).
15. Velsko, S. P. & Eimerl, D. Precise measurements of optical dispersion using a new interferometric technique. *Appl. Opt.* **25**, 1344–1349. https://doi.org/10.1364/AO.25.001344 (1986).
16. Fiebig, M., Fröhlich, D., Leute, S. & Pisarev, R. V. Topography of antiferromagnetic domains using second harmonic generation with an external reference. *Appl. Phys. B* **66**, 265–270. https://doi.org/10.1007/s003400050387 (1998).
17. Huang, J. Y. & Lewis, A. Determination of the absolute orientation of the retinylidene chromophore in purple membrane by a second-harmonic interference technique. *Biophys. J.* **55**, 835–842. https://doi.org/10.1016/S0006-3495(89)82883-8 (1989).
18. Kemnitz, K. et al. The phase of second-harmonic light generated at an interface and its relation to absolute molecular orientation. *Chem. Phys. Lett.* **131**, 285–290. https://doi.org/10.1016/0009-2614(86)87152-4 (1986).
19. Marowsky, G. & LuPke, G. CARS-Background suppression by phase-controlled nonlinear interferometry. *Appl. Phys. B Photophys. Laser Chem.* **51**, 49–51. https://doi.org/10.1007/bf00332324 (1990).
20. Geiger, F., Stolle, R., Marowsky, G., Palenberg, M. & Felderhof, B. U. Single-valued determination of second-order nonlinear susceptibilities by quarter-wave-plate rotation. *Appl. Phys. B Laser Opt.* **61**, 135–141. https://doi.org/10.1007/bf01090934 (1995).
21. Chen, Z. et al. Low-symmetry monoclinic phases and polarization rotation path mediated by epitaxial strain in multiferroic $BiFeO_3$ thin films. *Adv. Funct. Mater.* **21**, 133–138. https://doi.org/10.1002/adfm.201001867 (2011).
22. Kim KE, Jang BK, Heo Y, Hong Lee J, Jeong M, Le JY, Seidel J, Yang, C-H. Electric control of straight stripe conductive mixed-phase nanostructures in La-doped $BiFeO_3$. *NPG Asia Mater.* **6**, e81 (2014).
23. Cherifi-Hertel, S. et al. Non-ising and chiral ferroelectric domain walls revealed by nonlinear optical microscopy. *Nat. Commun.* **8**, 15768. https://doi.org/10.1038/ncomms15768 (2017).
24. Kumar, A. et al. Linear and nonlinear optical properties of $BiFeO_3$. *Appl. Phys. Lett.* **92**, 121915 (2008).
25. Marie Nelson C, Spies M, Abdallah LS, Zollner S, Xu Y, Luo H. Dielectric function of $LaAlO_3$ from 0.8 to 6 eV between 77 and 700 K. *J. Vacuum Sci. Technol. A* **30**, 061404 (2012).
26. Sando, D., Barthélémy, A. & Bibes, M. $BiFeO_3$ epitaxial thin films and devices: past, present and future. *J. Phys. Condens. Matter* **26**, 473201. https://doi.org/10.1088/0953-8984/26/47/473201 (2014).

Acknowledgements

This work was supported by the National Research Foundation of Korea (NRF) grant funded by the Korea government (MSIT) (No. 2022R1A2C2007847). C.-H.Y. acknowledges the support of the Korean government via the Creative Research Initiative Center for Lattice Defectronics (NRF grant No. 2017R1A3B1023686).

Author contributions

Y.J.J. and J.S.L. developed the research idea. Y.J.J. prepared the experimental setup and performed the second harmonic generation measurements together with I.H.C. and H.J.. Y.J.J. and D.G.J. analyzed the results. J.H.L. and C.H.Y. prepared the La-doped BFO sample. Y.J.J. and J.S.L. wrote the manuscript and discussed the results with input from all co-authors. The project was supervised by J.S.L.

Declarations

Competing interests

The authors declare no competing interests.

Additional information

Supplementary Information The online version contains supplementary material available at https://doi.org/10.1038/s41598-024-75597-6.

Correspondence and requests for materials should be addressed to J.S.L.

Reprints and permissions information is available at www.nature.com/reprints.

Publisher's note Springer Nature remains neutral with regard to jurisdictional claims in published maps and institutional affiliations.